BIOPHYSICS

Intracellular environment can change protein conformational dynamics in cells through weak interactions

Mengting Wang[1,2,3]†, Xiangfei Song[1,2]†, Jingfei Chen[1,2], Xiaoxu Chen[1,2,3], Xueying Zhang[1,2,3], Ying Yang[1,2], Zhijun Liu[4], Lishan Yao[1,2]*

Conformational dynamics is important for protein functions, many of which are performed in cells. How the intracellular environment may affect protein conformational dynamics is largely unknown. Here, loop conformational dynamics is studied for a model protein in *Escherichia coli* cells by using nuclear magnetic resonance (NMR) spectroscopy. The weak interactions between the protein and surrounding macromolecules in cells hinder the protein rotational diffusion, which extends the dynamic detection timescale up to microseconds by the NMR spin relaxation method. The loop picosecond to microsecond dynamics is confirmed by nanoparticle-assisted spin relaxation and residual dipolar coupling methods. The loop interactions with the intracellular environment are perturbed through point mutation of the loop sequence. For the sequence of the protein that interacts stronger with surrounding macromolecules, the loop becomes more rigid in cells. In contrast, the mutational effect on the loop dynamics in vitro is small. This study provides direct evidence that the intracellular environment can modify protein loop conformational dynamics through weak interactions.

INTRODUCTION

The interior of a cell is crowded with ions, metabolites, and macromolecules. Through excluded volume effect (*1*) or direct weak interactions (such as electrostatics, H-bonding, and stacking), which drive proteins to form quinary structures (*2*–*5*), the cellular environment can change protein diffusion (*6*–*9*), protein folding (*10*–*17*), and protein ligand binding (*18*–*24*). For intrinsically disordered proteins (IDPs), the excluded volume effect limits their conformational space so that they tend to adopt more compact conformations (*9*, *25*). For well folded proteins, the cellular environment may perturb local structures (*26*, *27*), but the overall protein structures are unchanged (*28*, *29*). The resolution of solved protein structures in cells (all by NMR) is not that high due to relatively short data acquisition time (limited by cell viability) and generally low signal-to-noise ratio (due to transient interactions with large molecules). More studies are needed to understand the exact cellular environmental effect on protein structures. On the other hand, proteins are not rigid structures. Protein dynamics through motions of loops, linkers, and hinges can generate distinctive conformations that are important for protein function (*30*, *31*). However, whether the cellular environment can modify protein conformational dynamics is largely unknown. NMR is a particularly powerful technique in studying molecules in cells at the atomic level [see, e.g., (*32*–*48*)], but studies of protein conformational dynamics in cells are sparse. Previously, we used the ^{15}N Carr-Purcell-Meiboom-Gill (CPMG) NMR relaxation dispersion method (*49*–*53*) to examine protein folding and unfolding exchange and found that folding of the studied protein is slowed down by the cellular environment (*54*). Here, we attempted to measure conformational dynamics of a protein in *Escherichia coli* cells and understand how weak interactions with the cellular environment may perturb protein dynamics.

^{15}N longitudinal (R_1), transverse (R_2) relaxation rates, and heteronuclear nuclear Overhauser effect (^{15}N-{^{1}H} NOE) measurements, coupled with the model-free analysis (*55*, *56*), are commonly used to study picosecond to nanosecond timescale protein backbone conformational dynamics in solution (*57*). However, the relatively poor NMR signal-to-noise ratio for proteins in cells hinders the accurate measurement of ^{15}N-{^{1}H} NOE, because the sensitivity of the NOE experiment is considerably lower than that of ^{15}N R_1 and R_2 measurements. Recently, Bruschweiler and coworkers have proposed an elegant NMR relaxation method where only R_2 rate is required to determine protein dynamics in picosecond to microsecond timescale with the assistance of silica nanoparticles (SNPs) (*58*–*61*). SNPs create a fast exchange for the protein between the bound and free form, which extends the overall protein tumbling time. The dynamics slower than the tumbling time of the free protein, which is usually not observable in the relaxation measurement, can be observed due to the extended tumbling time. Inspired by their work, here we determined conformational dynamics for a model protein in buffer and in cells. Together with ^{15}N CPMG NMR relaxation dispersion experiments (*52*, *53*) and backbone N-H residual dipolar coupling (RDC) measurements, the timescale of dynamics is characterized. It is shown that the protein loop dynamics in *E. coli* cells is perturbed by cellular environment. Specifically, weak attractive interactions between the loop and macromolecules in cells tend to suppress the loop dynamics.

[1]Qingdao New Energy Shandong Laboratory, Qingdao Institute of Bioenergy and Bioprocess Technology, Chinese Academy of Sciences, Qingdao 266101, China. [2]Shandong Energy Institute, Qingdao 266101, China. [3]University of Chinese Academy of Sciences, Beijing 100049, China. [4]National Facility for Protein Science, Shanghai Advanced Research Institute, Chinese Academy of Sciences, Shanghai 201210, China.
*Corresponding author. Email: yaols@qibebt.ac.cn
†These authors contributed equally to this work.

RESULTS

Backbone relaxation rates of a GB3 variant in buffer and in cells

GB3, the third immunoglobulin binding domain of protein G, is a small protein of 56 residues. Its dynamics has been studied by NMR ^{15}N relaxation (*62*) and RDC methods (*63*, *64*). The linkers G9-L12 and D40-G41 display elevated backbone dynamics. Here, the linker G9-L12 was converted to a longer loop by inserting a GNSGG sequence between K10 and T11. The amino acid sequence of the GB3 variant (named GB3L) is displayed in table S1, with the loop corresponding to residues G9-L17 (named loop 1). GB3L has an overall structure similar to the wild-type (WT) GB3, as indicated by the backbone ^{1}H-^{15}N RDCs (see discussion below).

Backbone amide ^{15}N R_1, $R_{1\rho}$, and ^{15}N-{^{1}H} NOE data were collected for GB3L at both 600 and 900 MHz fields (*65*, *66*) in the buffer of 40 mM bis-tris propane/40 mM Hepes (pH 6.8) (Fig. 1, A to C). From the NOE data, one can see that loop 1 and the linker D45-G46 (D40-G41 in GB3) show elevated conformational dynamics (see discussion below). The R_2 rates, derived from R_1 and $R_{1\rho}$ (*30*), indicate that D19 and T21 display conformational exchanges.

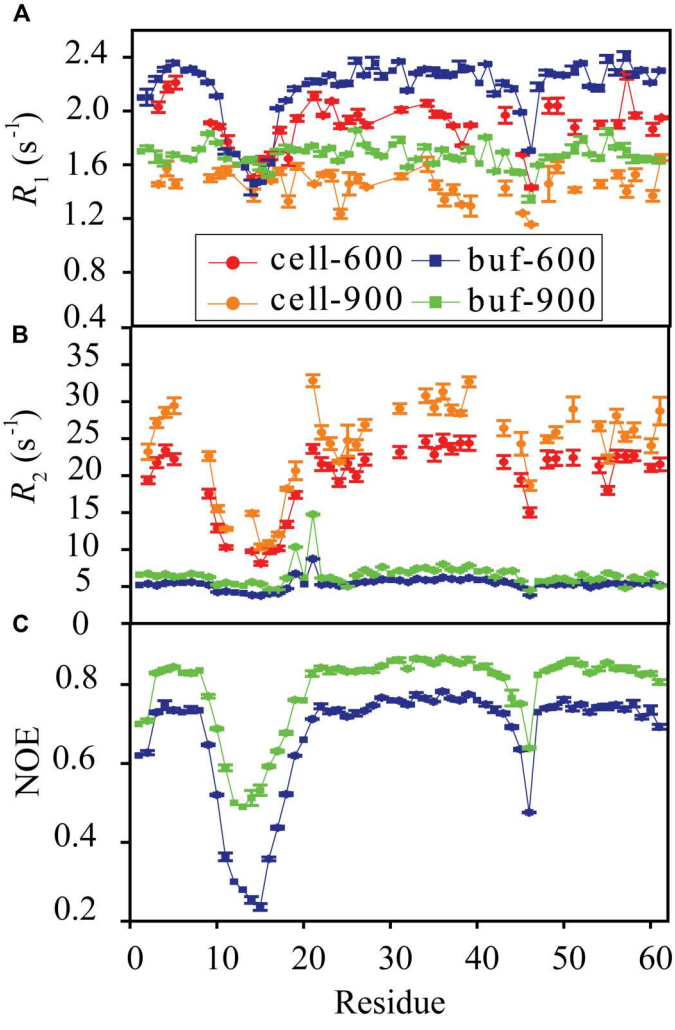

Fig. 1. Protein backbone amide relaxation rates. ^{15}N R_1 (**A**), R_2 (**B**), and ^{15}N-{^{1}H} NOE (**C**) were measured for GB3L at both 600 and 900 MHz fields in the buffer and in *E. coli* cells at 303 K. The pH in cells, monitored by using ^{15}N chemical shift of H33 (fig. S1), was adjusted to be the same as that in the buffer (40 mM bis-tris propane/40 mM Hepes, pH 6.8). Error bars are SEM (n = 3 independent experiments).

^{15}N R_1 and $R_{1\rho}$ data were also collected for GB3L in *E. coli* cells (Fig. 1, A and B). The pH in cells was monitored by using ^{15}N chemical shift of H33 (the only histidine residue in the protein). This chemical shift is sensitive to pH changes from ~6 to 8 presumably caused by the ionization state change of H33, based on the GB3L pH titration experiment in buffer (fig. S1). The ^{15}N chemical shift H33 in cells was matched to that in vitro [115.92 parts per million (ppm) at pH of 6.8] by adjusting the pH of the buffer (40 mM bis-tris propane/40 mM Hepes) used for cell suspension and in-cell NMR measurements (fig. S1). Therefore, the pH difference effect on dynamics and relaxation rates is eliminated. Compared to relaxation rates in the buffer, ^{15}N R_1s in cells are slightly smaller, whereas ^{15}N R_2s are considerably larger (Fig. 1B). To ensure that the relaxation rates were from GB3L in cells, a ^{1}H-^{15}N heteronuclear single-quantum coherence (HSQC) spectrum was collected after R_1 and $R_{1\rho}$ experiments (~3.5 hours). The protein concentration in the supernatant was very small (fig. S2), suggesting that the cell sample was stable during the relaxation measurements and signals were from GB3L in cells. The cells were viable after NMR experiments as proved previously (*67*).

Conformational dynamics (picosecond to nanosecond) of GB3L in the buffer

The model-free (*55*, *56*) analysis was performed to extract the diffusion tensor (table S2), the order parameter (Fig. 2A), and the internal correlation time τ_e (fig. S3) from R_1, R_2, and NOE data at 600 and 900 MHz fields. Most residues are quite rigid, especially those from the α-helix and β-strand secondary structures. Loop 1 (G9-L17) displays elevated dynamics, with the inserted GNSGG (G11-G15) fragment being particularly flexible (Fig. 2A). The linker D45-G46 also shows some flexibility, consistent with that of the WT GB3 (*62*). The conformational exchange rate R_{ex} was also extracted for D19 and T21, yielding values of 2 and 3.78 s^{-1}, respectively, at 600 MHz field (table S3), indicating that these two residues have conformational exchanges.

Conformational dynamics of GB3L in cells

The weak attractive interactions with larger molecules in cells are expected to increase ^{15}N R_2 rates (*68*) of GB3L. Meanwhile, R_2 rates can also be increased by higher viscosity in cells than that of water (*69*, *70*). For GB3L that binds transiently with surrounding molecules in cells, the ^{15}N R_2 rate for its backbone amide can be written as

$$R_{2,\mathrm{cell}} = \sum p_i R_{2i,\mathrm{cell}} \ (i = 0, 1, 2, \ldots) \quad (1)$$

where $i = 0$ ($i > 0$) corresponds to the free (bound) state, $R_{2i,\mathrm{cell}}$ is the GB3L backbone amide ^{15}N R_2 rate of state i (free GB3L or GB3L bound to different molecules in cells), and p_i is the state population ($\sum p_i = 1$). The equation is valid provided that the binding/unbinding rate is slower than the tumbling of GB3L (~10^9 s^{-1}), but much faster than the [^{1}H, ^{15}N] chemical shift differences between different states. To extract the dynamic information, ΔR_2 was introduced (see

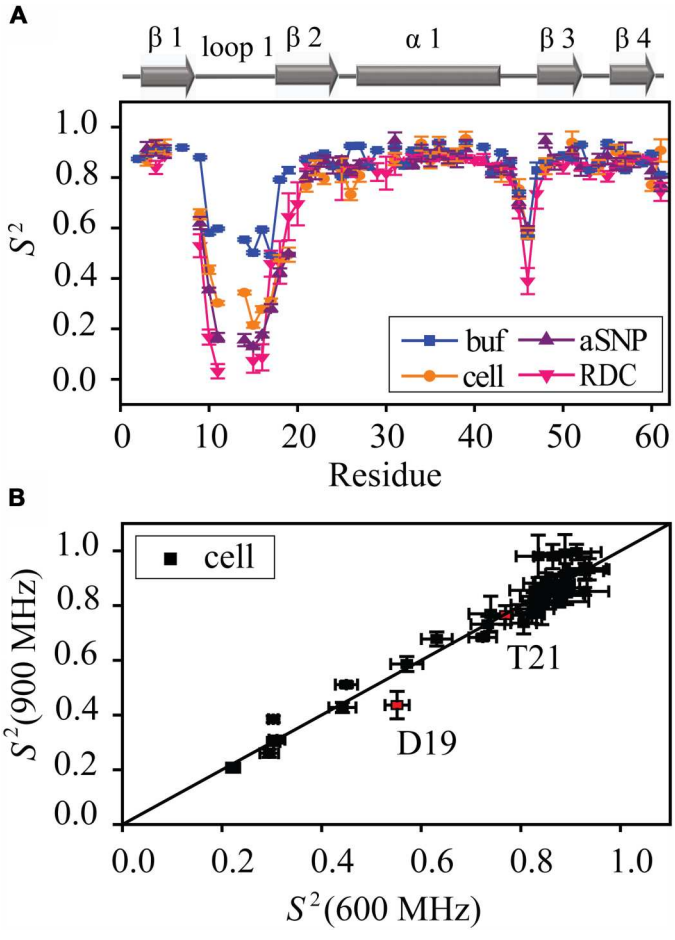

Fig. 2. Conformational dynamics of GB3L. (**A**) Order parameters in the buffer only, with anionic SNPs (aSNP), and in *E. coli* cells. The presence of anionic SNPs extends the dynamic observation time window so that picosecond to microsecond dynamics (S^2_{SNP}) can be detected, which is undetectable in the conventional model-free analysis of ^{15}N R_1, R_2, and NOE data measured in the buffer only (S^2_{buf}). GB3L S^2 in *E. coli* cells (S^2_{cell}) agrees better with S^2_{SNP}, suggesting that the dynamics detected in cells is probably on picosecond to microsecond timescale. Picosecond to millisecond timescale S^2 fitted from backbone amide ^{1}H-^{15}N RDCs (S^2_{RDC}) was also included (only residues with at least two sets of experimental RDCs are shown). (**B**) Correlation of S^2 in *E. coli* cells (S^2_{cell}) measured at 600 and 900 MHz fields. Two residues D19 and T21 show conformational exchanges (in red). Error bars (except for S^2_{RDC}) are SEM (n = 3 independent experiments). Error bars for S^2_{RDC} are SD from 10 independent ensemble fittings.

more details in the Supplementary Materials),

$$\Delta R_{2,\mathrm{cell}} = R_{2,\mathrm{cell}} - R_{2,\mathrm{buf}} \approx cS^2_{\mathrm{cell}}(\tau_{\mathrm{cell}} - \tau_{\mathrm{buf}}) \quad (2)$$

where $R_{2,\mathrm{buf}}$ is the GB3L backbone amide ^{15}N R_2 rate in the buffer, c is a constant, τ_{cell} is the GB3L average tumbling time in cells ($\tau_{\mathrm{cell}} = \sum p_i\tau_{i,\mathrm{cell}}$,$\tau_{i,\mathrm{cell}}$ is the tumbling time of state i), and τ_{buf} is the GB3L tumbling time in the buffer. S^2_{cell} is a weighted average of S^2 from different state i

$$S^2_{\mathrm{cell}} = \frac{\sum p_i S_i^2(\tau_{i,\mathrm{cell}} - \tau_{\mathrm{buf}})}{\sum p_i(\tau_{i,\mathrm{cell}} - \tau_{\mathrm{buf}})} \quad (3)$$

Extracting order parameters from ΔR_2 was first proposed by Bruschweiler and coworkers where SNPs were used to broaden NMR dynamic detection timescale (*58*–*60*). In the in-cell system, the situation is a bit more complicated because the macromolecules are more diverse and the viscosity is different in cells. It is worth mentioning that S^2_{cell} is not an arithmetic mean of S^2 of the free state and that of different bound states. It is a mean of S^2 weighted by the tumbling time difference between each state and that in the buffer. As the binding partner in cells becomes larger, its contribution to S^2_{cell} is more prominent. It is also noteworthy that Eq. 2 is an approximation and can be substituted by a treatment using a numerical stochastic Liouville equation provided that the exchange rates between different states are known (*71*).

To evaluate the applicability of Eq. 2, we used a simple two-state model, a free state and a bound state in cells, to simulate the impact of GB3L binding partner size, binding population, and viscosity in cells on the predicted S^2. $R_{2,\mathrm{buf}}$ at 600 MHz was calculated using the GB3L dynamic parameters (Fig. 2A, fig. S3, and table S2), which were extracted from the experimental relaxation data in the buffer using the model-free analysis (*55*, *56*). $R_{2,\mathrm{cell}}$ at 600 MHz was calculated using the same internal motion parameters but assuming that the viscosity in cells is 2.5 times that of water (*69*, *70*). The binding partner has a molecular weight (MW) of 50 kDa, the average MW of proteins in cells. Equation 2 was used to predict S^2 from the synthetic ΔR_2 data. The S^2 error is ~6% when there is only the free state in cells, and decreases quickly when the bound state increases (fig. S4A). The relatively large S^2 error of the free state is mainly caused by the axially symmetric diffusion tensor of free GB3L in buffer and in cells. If an isotropic diffusion tensor is assumed with the same tumbling time, the error is much smaller (fig. S4B). The S^2 error is not very sensitive to the MW of binding partner or viscosity in cells (fig. S4C). The data simulation suggests that Eq. 2 can be used to extract S^2 with good accuracy.

GB3L backbone amide R_2 rates in cells were determined at both 600 and 900 MHz fields (Fig. 1). S^2 in cells (S^2_{cell}) were extracted from ΔR_2 rates using Eq. 2 (Fig. 2A). The experimental ΔR_2 of ~18 s^{-1} (Fig. 1) at the 600 MHz field corresponds to a bound population of ~15% in the model, or S^2 error of ~2% (fig. S4A). The quality of S^2_{cell} is quite good, as suggested by the correlation between the values extracted independently from the two fields (Fig. 2B). Similar to S^2 in the buffer, order parameters in cells indicate that loop 1 and the linker D45-G46 display elevated dynamics. S^2_{cell} values of 0.75 and 0.58 for D45 and G46 are almost the same as those in the buffer (Fig. 2A). In comparison, loop 1 becomes more flexible in cells. Moreover, the residues next to loop 1 (including K18 and D19) are also more flexible, as if the dynamics of loop 1 and neighboring residues is boosted in cells. However, one needs to be careful that only order parameters of the internal dynamics faster than the tumbling time (3.5 ns) of GB3L can be extracted from ^{15}N R_1, R_2, and ^{15}N-{^{1}H} NOE data in the buffer. If loop 1 has dynamics slower than 3.5 ns, it might only be detectable in cells where binding to large molecules in cytosol increases GB3L tumbling time.

Conformational dynamics (picosecond to microsecond) of GB3L in the buffer with the assistance of SNPs

To capture the dynamics slower than nanoseconds in the buffer, colloidal anionic SNPs with a mean diameter of 20 nm were added to the buffer where backbone amide ^{15}N R_1 and R_2 rates

were collected and S^2 were extracted (fig. S5 and Fig. 2A) (*59*). The presence of SNPs increases the (bound) protein tumbling time to a few microseconds (*58*), thus broadening the detection limit of conformational dynamics. S^2 values of D45 and G46 are similar to those in the buffer without SNPs, suggesting that these two flexible residues have no nanosecond to microsecond dynamics. But the smaller S^2 values of loop 1 than those in the buffer in the absence of SNPs indicate that this loop has dynamics on nanosecond to microsecond timescale (*59*). The comparable dynamic amplitude for loop 1 in cells and in the buffer with SNPs suggests that the dynamics observed in cells is probably on the same timescale.

Conformational dynamics (picosecond to millisecond) of GB3L in the buffer from RDCs

To independently determine the conformational dynamics of GB3L in the buffer, backbone ^{1}H-^{15}N RDCs, which are sensitive to dynamics on picosecond to millisecond timescale, were measured from multiple alignments at 900 MHz field. Previously, we showed that five independent alignments could be obtained for GB3 by attaching a DO3MA-6MePy tag chelated with Tm^{3+} to K19C, V21C, K28C, Q32C, and D36C, respectively (*64*). For GB3L, attaching the tag to K24C and V26C was successful (corresponding to K19C and V21C in GB3). Attempts to attach the tag to the other three residues failed because these GB3L mutants were very unstable. Instead, we were able to attach the tag to A53C (of GB3L). Together with RDCs in the external alignment medium Pf1 (*72*), there are a total of four sets of ^{1}H-^{15}N RDCs for the protein (tables S4 and S5). Singular value decomposition analysis shows that the ratio between the largest singular value and the smallest one is 4:1, suggesting that four independent RDC datasets are present (Fig. 3A). All the mutation sites are away from loop 1 (Fig. 3B) so that these cysteine mutations should have a very small impact on its dynamics.

A protein ensemble fitting was performed using GB3L backbone ^{1}H-^{15}N RDCs. The average structure and order parameters S^2_{RDC} were calculated (Figs. 2 and 3B). The overall structure is very similar to that of GB3, except with an elongated loop 1 (Fig. 3B). S^2_{RDC} has a pattern similar to S^2_{SNP} (S^2 in the presence of SNPs; Fig. 2A). The elevated dynamics of loop 1 extracted from RDCs (compared to that from model-free analysis) independently validates the information extracted from ΔR_2 in SNPs that this loop has conformational dynamics slower than the protein tumbling time. The somewhat smaller S^2_{RDC} than S^2_{SNP} also indicates that this loop has a bit of microsecond to millisecond timescale dynamics (Fig. 2A), since the protein dynamics detected from the RDCs is on the picosecond to millisecond timescale, broader than that from ΔR_2 in SNPs. Furthermore, residue G46 has a S^2_{RDC} smaller than S^2_{SNP}, suggesting that this residue has dynamics on microsecond to millisecond timescale as well.

Millisecond dynamics of GB3L in buffer from CPMG measurements

As stated above, two residues D19 and T21 show conformational exchanges ($R_{ex} > 0$). ^{15}N CPMG NMR relaxation dispersion experiments (*52*, *53*) were performed for GB3L at both 600 and 900 MHz fields to see whether the conformational exchange persists for the protein on the millisecond timescale. Dozens of residues (including D19 but not T21) display some (albeit small) exchanges as suggested by the apparent ^{15}N R_2 relaxation rate differences at different 180° ^{15}N CPMG pulsing frequencies (Fig. 4A). A two-site model was assumed where a global fitting was performed for 25 exchanging residues to extract the exchange rates (k_1 and k_{-1}) and the chemical shift difference ($\Delta\omega_{CPMG}$). $\Delta\omega_{CPMG}$ is correlated with the chemical shift difference between the unfolded and folded GB3L (Fig. 4B and fig. S6), suggesting that the exchange process corresponds to GB3L folding and unfolding. The relatively slow exchange rate ($k_1 + k_{-1} = 400\ s^{-1}$) and the low population of the unfolded state (0.5%) indicate that the contribution of the folding-unfolding exchange to ^{15}N $R_{1\rho}$ rates is very small (Fig. 4, C and D). Thus, its impact on the model-free and ΔR_2 analyses is expected to be small as well. This exchange process is not pursued any further.

Mutational effect on GB3L dynamics in buffer and in cells

Weak interactions with large molecules increase the detection time window of R_2 relaxation experiments in cells. One important question is whether the weak interactions affect loop dynamics in cells. To address this question, several mutations were prepared by changing X in the inserted GXSGG sequence to F, L, V, K, S, and D (N in GB3L). The order parameters for all the mutants in the buffer and in cells were extracted from relaxation rates (Fig. 5A and figs. S7 and S8). The loop 1 order parameters S^2 of different mutants are compared to see how the loop sequence modulates its dynamics. The average loop order parameter (averaged over G11-L17, excluding residues X12 and S13, which have S^2 missing due to signal overlapping in certain mutants) variation in the buffer from model-free analyses is relatively small (Fig. 5B). In contrast, the results in cells show that $\langle S^2_{cell}\rangle$ varies quite a bit, depending on the X amino acid type, generally in the order of hydrophobic > positively charged > polar and negatively charged amino acid (Fig. 5). The most rigid loop (F mutant) has an $\langle S^2_{cell}\rangle$ ~60% higher than the most flexible one (D mutant) in cells. Furthermore, a positive correlation can be seen between the average order parameter and the average ΔR_2 of rigid GB3L residues (Fig. 5C). Increase of the average ΔR_2 can be caused by the population increase of the bound states due to the loop stronger interactions with surrounding macromolecules in cells (see Eq. 1). The positive correlation indicates that the loop becomes more rigid as the interactions become stronger. In other words, the loop attractive interactions with intracellular macromolecules tend to suppress GB3L loop dynamics in cells. It is worth mentioning that increasing the bound population alone (which increases ΔR_2) does not affect loop S^2 if the free and bound forms have identical S^2 values (Eq. 3). On the basis of the GXSGG mutational effect on $\langle\Delta R_2\rangle$, hydrophobic interactions contribute the most to the loop surrounding interactions, followed by electrostatic attraction between the positively charged loop (as in GKSGG) and generally negatively charged proteins in *E. coli*. These two types of interactions have the largest effect on S^2 (Fig. 5C). On the other hand, the electrostatic repulsion with the negatively charged loop (GDSGG) affects the loop dynamics the least. This may also explain that the dynamics of the loop D45-G46 in cells is very similar to that in the buffer (Fig. 5A). As for the whole protein that has both charged and hydrophobic residues on the surface, it is hard to tell whether hydrophobic or electrostatic interactions with cellular environment are more important.

The order parameters S^2_{SNP} of different mutants were also determined in the presence of SNPs (Fig. 5A and fig. S9). The loop 1 S^2_{SNP} of F, S, and D mutants is ~0.2, comparable with GB3L (N; Fig. 5B), but that of L and V mutants is ~50% larger and the K mutant has the

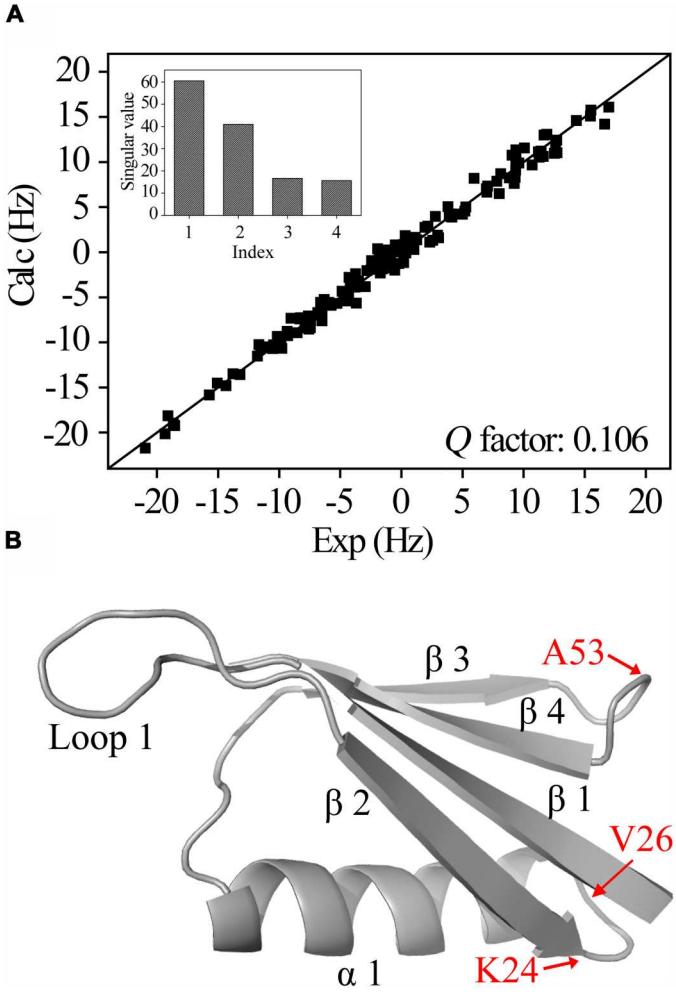

Fig. 3. Ensemble fitting of GB3L backbone ^{1}H-^{15}N RDCs. A total of four sets of RDCs were measured at 900 MHz, with three from DO3MA-6MePy-Tm^{3+} attached to K24C, V26C, or A53C, and one from the external alignment medium Pf1. The x-ray structure of GB3 [pdb code: 2OED (*87*)] with the inserted loop was used as the starting structure for molecular dynamic simulation to generate an ensemble of eight structures for the experimental RDC fitting. (**A**) Correlation between experimental and back-calculated RDCs from the ensemble, and singular value decomposition of experimental RDCs, which was used to yield singular values (panel insert) and check the independence of RDCs (see more details in the main text). (**B**) Ensemble averaged structure displayed with the pointed DO3MA-6MePy-Tm^{3+} attaching sites. The order parameter S^2_{RDC} is displayed in Fig. 2A for comparison with S^2 from the other methods.

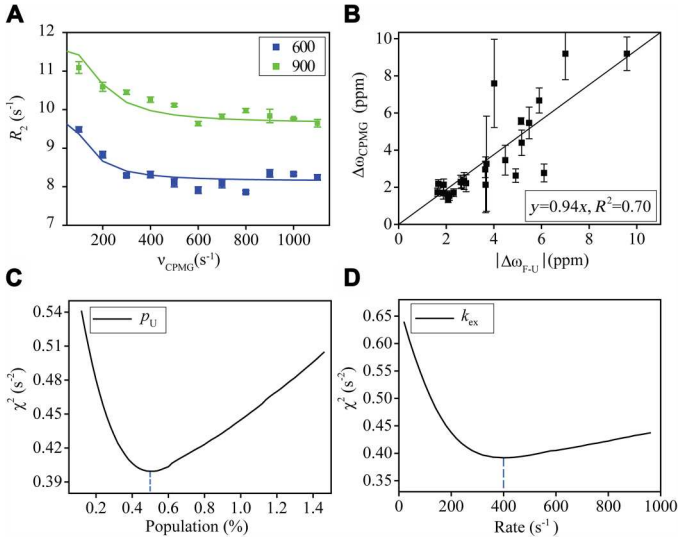

Fig. 4. ^{15}N CPMG NMR relaxation dispersion data analysis for GB3L. The data were measured in the buffer of 40 mM bis-tris propane/40 mM Hepes, pH 6.8, at 303 K. A two-site exchange model was used to fit the CPMG data for 25 residues that show chemical exchanges. (**A**) CPMG profile of A39 and its fitting curves. (**B**) Correlation between $\Delta\omega_{CPMG}$, the chemical shift difference from the fitting, and $\Delta\omega_{F-U}$, the chemical shift difference (absolute value) between the folded and unfolded GB3L. (**C**) Reduced χ^2 error versus the fitted unfolded state population. (**D**) χ^2 error versus the fitted exchange rate. The positive correlation between $\Delta\omega_{CPMG}$ and $\Delta\omega_{F-U}$ (absolute value) indicates that the conformational exchange corresponds to the protein folding and unfolding process. Error bars are SEM (n = 3 independent experiments).

largest loop 1 S^2_{SNP} (~140% larger than GB3L). It is noteworthy that weak interactions between the protein and anionic SNPs also exist (especially electrostatics), which can also perturb loop dynamics, as suggested by the positive correlation between ΔR_2 in anionic SNPs and S^2_{SNP} of loop 1 (fig. S10). In particular, the K mutant has the most rigid loop 1 and highest ΔR_2. The particularly large ΔR_2 may arise from the cooperative binding between K10 and K12 to SNPs (*73*). To understand the role of electrostatics, S^2 of the K mutant was determined from ΔR_2 in the buffer with neutral SNPs (Fig. 6A and figs. S11 and S12), which should diminish the SNPs' electrostatic attraction with the positively charged loop lysine residue. As can be seen, the average order parameter S^2 of loop 1 drops to 0.28, a 35% decrease compared to that from the anionic SNPs (Fig. 6B). Similarly, adding 200 mM (final concentration) lysine amino acid to the K mutant sample in the presence of anionic SNPs also decreases the order parameter of loop 1 roughly by the same percentage (the pH was adjusted to be the same as that without lysine). Meanwhile, $<\Delta R_2>$ of the rigid residues decreases by ~11%, suggesting that the interaction between the K mutant and anionic SNPs is weakened by free lysine amino acid. The abundant free lysine amino acid likely competes with the loop for the anionic SNPs. These results provide direct evidence that the electrostatic attraction between the K mutant loop and anionic SNPs rigidifies loop 1.

Although the model-free analysis shows that the mutational effect on loop 1 dynamics on picosecond to nanosecond timescale is rather small in the buffer, it is important to see how the mutations may affect dynamics on a slower timescale. In neutral SNPs, the K mutant still shows an average loop 1 S^2 (close to that of L and V mutants) ~50% higher than GB3L and the other mutants (Fig. 5B). But this dynamics difference may arise from the weak interactions with SNPs. To see how the K mutation may affect loop dynamics without SNPs, four sets of ^{1}H-^{15}N RDCs (same as those for GB3L) were measured for the mutant and the order parameters were determined through ensemble fitting (Fig. 7A). For loop 1, S^2_{RDC} of the K mutant is much smaller than S^2_{SNP} (Fig. 7B), but comparable with S^2_{RDC} of GB3L (Fig. 2A). The order parameter of the V mutant was also determined from RDCs (Fig. 7C), and a similar loop S^2_{RDC} to that of GB3L was obtained. Again, for this mutant, the loop S^2_{RDC} is smaller than S^2_{SNP} (Fig. 7D). Together, these

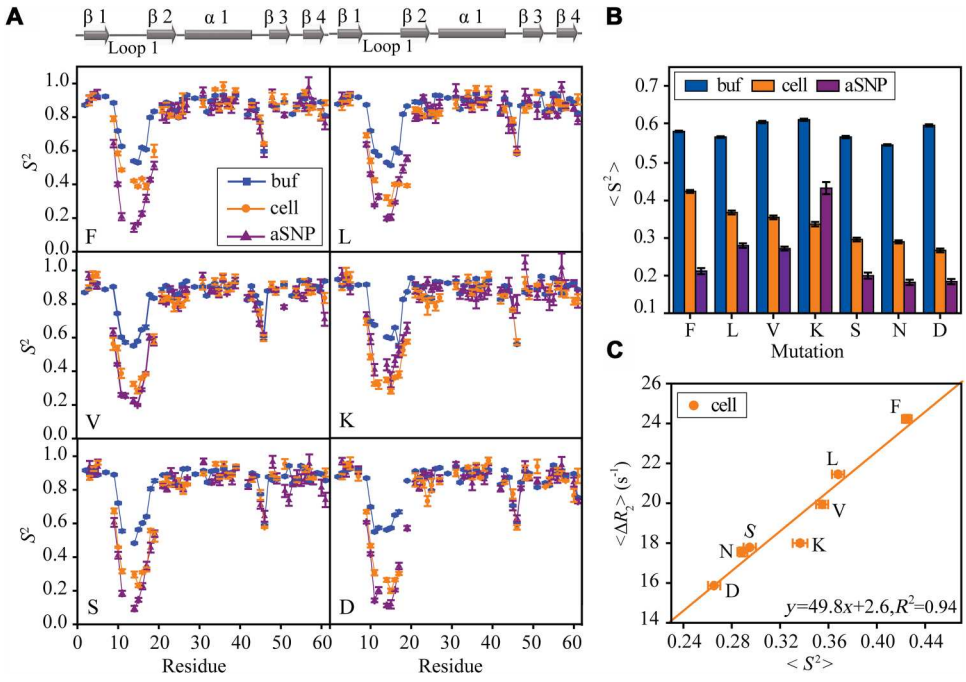

Fig. 5. GB3L conformational dynamics and its sequence dependence. The loop 1 sequence was varied by changing X in GXSGG to different amino acids. (**A**) S^2 order parameters for different mutants, F, L, V, K, S, and D. (**B**) Averages of loop S^2 (including G11, G14, G15, T16, and L17, which have S^2 values in all GB3L variants) of different mutants in the buffer only, in the presence of anionic SNP, and in cells. The loop S^2 average in cells (**C**) is correlated with $<\Delta R_2>$ [$\Delta R_2 = R_2$(cell) − R_2(buffer)] averaged over rigid GB3L residues. Error bars are SEM (n = 3 independent experiments).

results indicate that the larger loop S^2_{SNP} for the K and V mutants (Fig. 5B) is most likely caused by protein weak interactions with SNPs, whereas the mutational effect on loop dynamics is small, consistent with that from the model-free analysis.

DISCUSSION

Here, we studied the conformational dynamics of an inserted loop (loop 1) of GB3L in the buffer and in *E. coli* cells. The model-free analysis of ^{15}N R_1, R_2, and NOE in the buffer suggests that loop 1 and a few neighboring residues have elevated dynamics on picosecond to nanosecond timescale (Fig. 2A). As demonstrated by Leeb and colleagues (*68*), the average protein amide ^{15}N R_1, R_2 relaxation rates in cells, measured using 1D ^{15}N-filtered HSQC-based pulse sequences, can be interpreted by a chemical exchange model, between the free and the bound forms to some large molecules. Because of complexity of cellular environment, there are likely many different bound forms. The simplest case is that only one free form and one bound form exist, as in the buffer with SNPs. Binding to large molecules slows down protein tumbling and thus broadens the conformational dynamic detection time window of the R_2 relaxation measurements. By taking this advantage, picosecond to microsecond timescale dynamics can be captured from ΔR_2. With the assistance of SNPs, conformational dynamics on picosecond to microsecond timescale was observed for loop 1. S^2_{SNP} extracted from ΔR_2 using SNPs agrees reasonably well with that from RDCs, which are sensitive to dynamics up to milliseconds (Figs. 2A and 3). S^2_{cell} of GB3L (GNSGG) has a profile similar to that in the buffer S^2_{SNP} (Fig. 2A). In other words, the loop picosecond to microsecond dynamics in cells is consistent with that detected in the buffer by nanoparticle-assisted spin relaxation measurements and RDCs, which, in our opinion, validates the method used in this work. A folding-unfolding conformational exchange has been shown for the overall protein, with the population of the unfolded protein ~0.5% and the exchange rate ~400 s^{-1} (Fig. 4). The impact of the exchange on loop dynamics is very small.

To extract S^2_{cell} from ΔR_2, one assumption is made that the exchange contribution to R_2 in the buffer and in *E. coli* cells needs to cancel out each other. Taking residues D19 and T21 as an example, both residues have obvious conformational exchanges (positive R_{ex}) in the buffer (Fig. 1). R_{ex} can be altered if the molecules in cells interact differently with the ground state and the excited state. For the fast conformational exchange with R_{ex} proportional to the square of the field strength, as observed for D19 and T21 of GB3L, the change of R_{ex} would affect ΔR_2 and thus S^2_{cell} at the 900 MHz field differently from that at the 600 MHz field (eqs. S2 and S3). If R_{ex}(cell) > R_{ex}(buffer), S^2_{cell} at 900 MHz will be overestimated more than that at 600 MHz. Otherwise, if R_{ex}(cell) < R_{ex}(buffer), S^2_{cell} at 900 MHz will be underestimated more than that at 600 MHz. For T21, S^2_{cell} at both fields matches well (Fig. 2B). For D19, S^2_{cell} at 900 MHz is a bit smaller than that at 600 MHz. But the deviation is only about two times the measurement error. Thus, we think that the impact of cellular environment on R_{ex} is relatively small for both residues. It is important to have S^2_{cell} from the two fields to validate the assumption.

Mutations on loop 1 have a big impact on $<S^2_{cell}>$, but their effect on $<S^2_{buf}>$ is small (Figs. 5 and 7). A positive correlation is shown between $<S^2_{cell}>$ and $<\Delta R_2>$. A similar correlation is shown between $<S^2_{SNP}>$ and $<\Delta R_2>$. The correlation is interpreted as that the loop becomes more rigid by interacting stronger with SNPs (Fig. 6) or

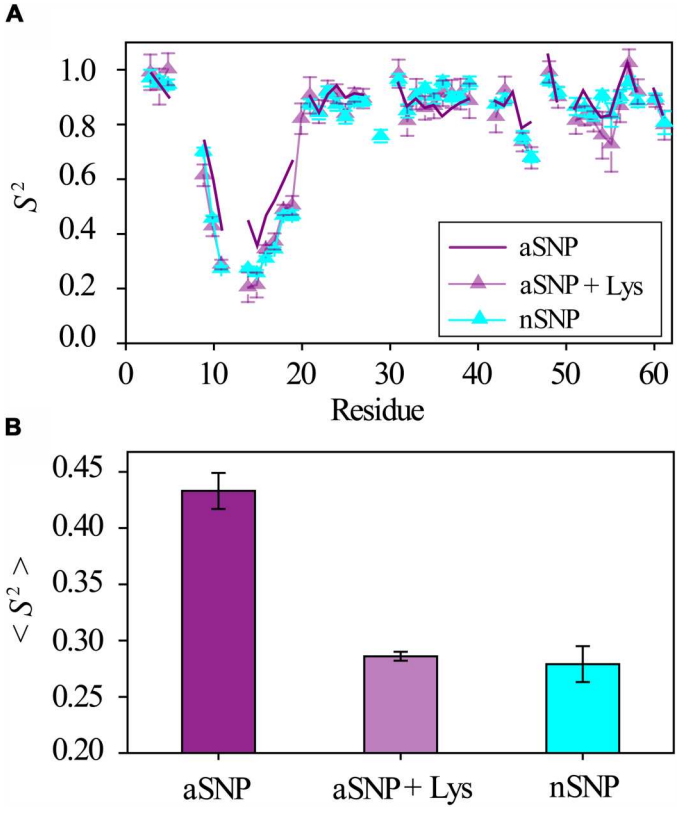

Fig. 6. Impact of SNPs on the conformational dynamics. (**A**) Order parameters S^2 of the GB3L K mutant measured in 40 mM bis-tris propane/40 mM Hepes, at pH 6.8 and 303 K. (**B**) The average S^2 of loop 1 is smaller with additional 200 mM lysine in the anionic SNPs (aSNP) at the same pH and temperature. A similar decrease was seen in the same buffer but with neutral SNPs (nSNP). It is apparent that the electrostatic attraction between the GKSGG loop and anionic SNPs suppresses the loop dynamics. Error bars are SEM (n = 3 independent experiments).

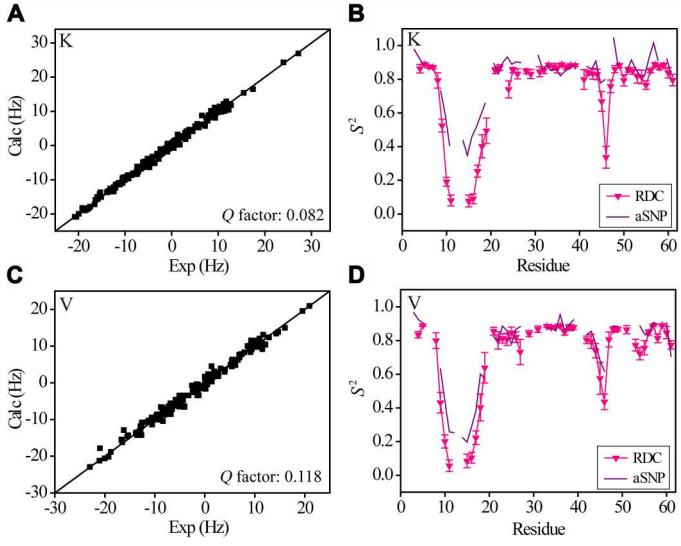

Fig. 7. Order parameters derived from ensemble fitting of backbone ^{1}H-^{15}N RDCs. A total of four sets of RDCs were measured and fitted in the same way for GB3L. (**A** and **C**) Correlation between experimental and back-calculated RDCs (for K and V mutants) from the ensemble. (**B** and **D**) Dynamics (S^2_{RDC}) calculated from the structure ensemble for the two mutants (only residues with at least two sets of RDCs are shown). S^2_{SNP} is also displayed for comparison. Error bars are SD from 10 independent ensemble fittings.

macromolecules in cells. This is not that surprising because binding of the protein to macromolecular surfaces can hinder the motion of the loop and thus decrease its flexibility. However, the cellular environment is rather complex, composed of various proteins, RNAs, and DNAs. The size and concentration distribution of the in-cell proteins are unknown. If the timescale range detected by NMR in cells is different for different mutants due to their binding to macromolecules with different sizes, the situation becomes more complicated. Therefore, it is assumed that the NMR detected motion timescale range is insensitive to mutations. One scenario is that, compared to GB3L, the mutants may bind to larger macromolecules stronger in cells, which will increase $<\Delta R_2>$ of the rigid residues as well (eq. S5). The binding helps NMR to detect a slower timescale motion. On the basis of the fact that loop 1 has dynamics on the microsecond to millisecond timescale, this will further decrease loop S^2, meaning that $<S^2>$ and $<\Delta R_2>$ should be negatively correlated, opposite to the experimental observation. Another scenario is that hydrophobic or positively charged mutants bind stronger to smaller macromolecules but similarly to larger macromolecules compared to the WT. The stronger binding gives larger ΔR_2 and larger S^2_{cell} as well (due to the narrower NMR detection timescale range), which would yield the same correlation as in Fig. 5C. One would expect that the attractive interactions with surrounding macromolecules are determined by their surface property, not their sizes. However, further studies are needed to investigate this scenario.

^{15}N R_1, R_2, and ^{15}N-{^{1}H} NOE rates have been measured before in *E. coli* cells at 700 MHz field and 298 K for phenylalanyl-glycyl-repeat–rich nucleoporins (FG Nups), which are IDPs (*74*). It has been suggested that "The cellular milieu maintains FG Nups as highly dynamic IDPs" (*74*). It is worth noting that the dynamic interpretation of the relaxation data of IDPs is far more complex than that of folded proteins. Relaxation rates measured at multiple fields are required to accurately quantify dynamics of IDPs (*75*). It is likely that weak interactions with cellular environment may suppress IDP dynamics as well. But a more thorough study is needed to address this issue.

The biomolecules in the interior of *E. coli* cells can reach 400 g/liter (*76*), which provides rich binding partners for proteins through weak attractive interactions. The weak interactions with intracellular environment can hinder protein loop dynamics. As the interactions increase, the impact on loop conformational dynamics becomes more prominent. This work highlights the role of intracellular environment on conformational dynamics and underlines the importance of direct dynamics study in cells. All biological functions are driven by interactions. The protein interactions with cellular environment have been shown to affect protein conformation (*9*, *23*, *27*–*29*), folding and stability (*11*, *12*, *14*, *16*, *40*), and protein-protein binding (*18*, *20*–*22*) in cells. Here, we showed that the interactions also affect protein loop dynamics. Many loop dynamics important for protein functions (e.g., enzyme catalysis and signal transduction) have been elucidated (*30*, *31*). We expect that the change on loop dynamics by cellular environment can affect protein functions in cells as well.

MATERIALS AND METHODS

Sample preparation for in vitro NMR experiments

The GB3L and its mutants were cultured and purified according to our previously described method (*77*). NMR samples were obtained by dissolving ~1.2 mM ^{15}N-labeled GB3 mutants in 600 μl of buffer, which is 40 mM bis-tris propane/40 mM Hepes at pH 6.8 [80%/20% (v/v) H_2O/D_2O]. Colloidal anionic and neutral SNPs, with an average diameter of 20 and 34 nm, respectively (product names Levasil CS40-120 and CC503), were purchased from AkzoNobel. The SNPs were dialyzed against 20 mM Hepes buffer (pH 6.8) using concentrator tubes with a MW cutoff of 10 kDa. The dialyzed anionic (neutral) SNPs were 20 (*5*) times diluted and mixed with GB3L and various mutants to prepare the NMR experiment samples with the same conditions as before (*58*). The samples of DO3MA-6MePy-Tm^{3+} attached GB3L mutants were prepared as described previously (*64*). Because of instability of GB3L and different mutants, the protein DO3MA-6MePy-Tm^{3+} tag chelating condition was modified by decreasing the temperature to 30°C.

Sample preparation for in-cell NMR experiments

The in-cell experiments were prepared as previously described with some modifications (*54*). *E. coli* BL21 (DE3) cells containing plasmids encoding different mutants of GB3L were cultured in 250 ml of LB medium at 37°C until $OD_{600} \approx 0.6$. The viable cells were centrifuged at 1000*g*, 4°C for 20 min. The obtained pellet was gently resuspended to 250 ml of ^{15}N-labeled M9 medium to cultured (37°C, 200 rpm, 30 min). Then, the *E. coli* cells were induced by additions of isopropyl-β-D-thiogalactopyranoside (with a final concentration of 0.2 mM) and cultivated for 1.5 hours. Finally, the viable cells were collected by centrifugation (1000*g*, 4°C, 20 min) and pipetted into the NMR tubes for NMR analysis {40 mM bis-tris propane/40 mM Hepes, pH 7.8 [80%/20% (v/v) H_2O/D_2O], in 600 μl volume}. Viability of *E. coli* cells was also verified by plating a sample in NMR tube before the measurement and 4 hours later (the total NMR measurement time is 3.5 hours). The colony numbers in two plates were comparable after 15 hours of incubation (fig. S13), suggesting that the cells were still viable after the NMR experiment.

NMR experiments and data analysis

All experimental data were collected at 303 K. A set of three-dimensional HNCACB and CBCA(CO)NH experiments was collected for ^{15}N/^{13}C-labeled GB3L (GNSGG) to confirm the ^{1}H-^{15}N HSQC assignment (*78*). ^{15}N spin relaxation (R_1 and $R_{1\rho}$) experiments were performed for GB3L in cells and in the buffer at 600 and 900 MHz (*79*). The R_1 and $R_{1\rho}$ rates for GB3L in the buffer with SNPs were measured at 600 MHz using the same method. The $R_{1\rho}$ relaxation delay intervals were [0.004, 0.01, 0.015, 0.02, 0.03 s] for GB3L in cells and for proteins in the buffer with SNPs. The $R_{1\rho}$ relaxation delay intervals were [0.004, 0.02, 0.04, 0.08, 0.12 s] at 600 MHz and [0.004, 0.01, 0.02, 0.04, 0.06 s] at 900 MHz for proteins in the buffer without SNPs. The spin-lock field strength is 2765 Hz at 600 MHz field and 1584 Hz at 900 MHz field. For all the R_1 measurements, the relaxation delays were [0.1, 0.2, 0.3, 0.4, 0.5, 0.6 s]. NOE experiments were performed in the buffer with the water flip-back scheme (*65*) and a recycling delay of 5.0 s. All the relaxation measurements were performed in triplicates. For measurements in the buffer without SNPs, the same sample was used. For measurements in the buffer with SNPs and in cells, three samples were prepared independently. The intracellular pH was maintained at pH 6.8, indicated by the chemical shift of H33 (fig. S1). The ^{1}H-^{15}N RDCs were measured using ^{1}H-^{15}N IPAP (In-phase Antiphase)-HSQC experiments (*80*), for GB3L with the residue K24C, V26C, or A53C mutation attached to DO3MA-6MePy-Tm^{3+} tag, or aligned in Pf1 (~10 g/liter) (*72*). Same measurements were performed for the K and V mutants. The data of CPMG were collected in the same way as previously described (*77*).

The transverse spin relaxation rate (R_2) was extracted according to

$$R_2 = R_{1\rho}/\sin^2\theta - R_1/\tan^2\theta \quad (4)$$

where $\theta = \arctan(\Omega/\omega)$, Ω is the chemical shift of each amino acid from the center position, and ω is the spin-lock field strength.

S^2 of each GB3L mutant in the buffer was obtained by model-free (*55*, *56*) fitting using a total of six sets of R_1, R_2, and NOE data at 600 and 900 MHz fields. The extended model with S^2_{fast}, S^2_{slow} ($S^2 = S^2_{fast}S^2_{slow}$), and an internal correlation time τ_e were used (*81*). For D19 and T21 that have conformational exchanges, an additional parameter R_{ex}, which is assumed proportional to the square of magnetic field strength, was included in the model-free fitting. An effective N-H bond length of 1.04 Å was used for the dipole-dipole spectra density calculation. ^{15}N Chemical Shift Anisotropy (CSA) tensor with (σ_{XX}, σ_{YY}, σ_{ZZ}) values of (71, 44, −115) ppm for α-helix residues, (70, 38, −108) ppm for β-strand residues, and (69, 42, −111) ppm for all other residues, were used in the fitting (*82*). The errors for S^2, τ_e, and R_{ex} were obtained from Monte-Carlo simulation by adding random noise to R_1, R_2, and NOE data. The SD of the R_1, R_2, and NOE random noise corresponds to the measured SEM of R_1, R_2, and NOE from triplicate measurements, respectively. The order parameters in cells were extracted from ΔR_2 as follows. The average model-free S^2 was calculated for protein rigid residues in the buffer. Then, the scaling factor k was calculated from eq. S7. A small correction was applied to k, because slightly different ^{15}N CSA tensors were used for different secondary structure residues, which slightly changed the constant c. The order parameters in cells were obtained from ΔR_2 and k, with $S^2_{cell} = \Delta R_2/k$. S^2_{cell} in cells at the two fields were averaged. The order parameters in the buffer with SNPs were obtained in the same way. All the dynamic analyses were performed using in-house programs.

Ensemble fitting of ^{1}H-^{15}N RDCs

The ensemble fitting of ^{1}H-^{15}N RDCs was performed using the GROMACS software (*83*), similar to the procedure in our previous work (*64*) and in the literature (*84*). The starting coordinates were generated from the RDC refined x-ray structure (2OED), by inserting the GXSGG loop between K10 and T16 using the Rosetta remodel application (*85*). The system was solvated in cubic boxes with 12.5 Å TIP3P waters. One-nanosecond molecular dynamic (MD) simulation was carried out at 350 K to equilibrate the system, after 5000 steps of energy minimization and 200 ps restrained (protein backbone heavy atoms only) NVT simulation using a force constant of 1000 kJ/ mol·nm^2. The MD snapshots were saved every 10 ps. The last 800 ps (a total of 80) MD snapshots were divided into 10 groups and used as the starting ensemble structures for RDC fitting. Ten ensemble refinements were carried out

with a force constant of 0.4 kJ/mol·Hz^2 with a simulated annealing process from 350 K to 0 K (*84*). The order parameters S^2 and average structure were calculated for each ensemble (*86*) and averaged over 10 ensembles.

Supplementary Materials

This PDF file includes:

Supplementary Text
Figs. S1 to S13
Tables S1 to S5
References

View/request a protocol for this paper from *Bio-protocol*.

REFERENCES AND NOTES

1. H. Reiss, H. L. Frisch, J. L. Lebowitz, Statistical mechanics of rigid spheres. *J. Chem. Phys.* **31**, 369–380 (1959).
2. E. H. Mcconkey, Molecular evolution, intracellular organization, and the quinary structure of proteins. *Proc. Natl. Acad. Sci. U.S.A.* **79**, 3236–3240 (1982).
3. A. J. Wirth, M. Gruebele, Quinary protein structure and the consequences of crowding in living cells: Leaving the test-tube behind. *Bioessays* **35**, 984–993 (2013).
4. R. D. Cohen, G. J. Pielak, A cell is more than the sum of its (dilute) parts: A brief history of quinary structure. *Protein Sci.* **26**, 403–413 (2017).
5. M. Gruebele, G. J. Pielak, Dynamical spectroscopy and microscopy of proteins in cells. *Curr. Opin. Struct. Biol.* **70**, 1–7 (2021).
6. Q. Wang, A. Zhuravleva, L. M. Gierasch, Exploring weak, transient protein–protein interactions in crowded in vivo environments by in-cell nuclear magnetic resonance spectroscopy. *Biochemistry* **50**, 9225–9236 (2011).
7. C. Kyne, P. B. Crowley, Short arginine motifs drive protein stickiness in the Escherichia coli cytoplasm. *Biochemistry* **56**, 5026–5032 (2017).
8. X. Mu, S. Choi, L. Lang, D. Mowray, N. V. Dokholyan, J. Danielsson, M. Oliveberg, Physicochemical code for quinary protein interactions in Escherichia coli. *Proc. Natl. Acad. Sci. U.S.A.* **114**, E4556–E4563 (2017).
9. I. Konig, A. Soranno, D. Nettels, B. Schuler, Impact of in-cell and in-vitro crowding on the conformations and dynamics of an intrinsically disordered protein. *Angew. Chem. Int. Ed. Engl.* **60**, 10724–10729 (2021).
10. A. P. Schlesinger, Y. Q. Wang, X. Tadeo, O. Millet, G. Pielak, Macromolecular crowding fails to fold a globular protein in cells. *J. Am. Chem. Soc.* **133**, 8082–8085 (2011).
11. W. B. Monteith, G. J. Pielak, Residue level quantification of protein stability in living cells. *Proc. Natl. Acad. Sci. U.S.A.* **111**, 11335–11340 (2014).
12. W. B. Monteith, R. D. Cohen, A. E. Smith, E. Guzman-Cisneros, G. J. Pielak, Quinary structure modulates protein stability in cells. *Proc. Natl. Acad. Sci. U.S.A.* **112**, 1739–1742 (2015).
13. J. Danielsson, X. Mu, L. Lang, H. Wang, A. Binolfi, F. X. Theillet, B. Bekei, D. T. Logan, P. Selenko, H. Wennerström, M. Oliveberg, Thermodynamics of protein destabilization in live cells. *Proc. Natl. Acad. Sci. U.S.A.* **112**, 12402–12407 (2015).
14. R. D. Cohen, G. J. Pielak, Electrostatic contributions to protein quinary structure. *J. Am. Chem. Soc.* **138**, 13139–13142 (2016).
15. S. Sukenik, M. Salm, Y. H. Wang, M. Gruebele, In-cell titration of small solutes controls protein stability and aggregation. *J. Am. Chem. Soc.* **140**, 10497–10503 (2018).
16. D. Gnutt, S. Timr, J. Ahlers, B. König, E. Manderfeld, M. Heyden, F. Sterpone, S. Ebbinghaus, Stability effect of quinary interactions reversed by single point mutations. *J. Am. Chem. Soc.* **141**, 4660–4669 (2019).
17. T. Sorensen, S. Leeb, J. Danielsson, M. Oliveberg, Polyanions cause protein destabilization similar to that in live cells. *Biochemistry* **60**, 735–746 (2021).
18. Y. Phillip, V. Kiss, G. Schreiber, Protein-binding dynamics imaged in a living cell. *Proc. Natl. Acad. Sci. U.S.A.* **109**, 1461–1466 (2012).
19. L. M. Luh, R. Hänsel, F. Löhr, D. K. Kirchner, K. Krauskopf, S. Pitzius, B. Schäfer, P. Tufar, I. Corbeski, P. Güntert, V. Dötsch, Molecular crowding drives active Pin1 into nonspecific complexes with endogenous proteins prior to substrate recognition. *J. Am. Chem. Soc.* **135**, 13796–13803 (2013).
20. Y. Yang, S. N. Chen, F. Yang, X. Y. Li, A. Feintuch, X. C. Su, D. Goldfarb, In-cell destabilization of a homodimeric protein complex detected by DEER spectroscopy. *Proc. Natl. Acad. Sci. U.S.A.* **117**, 20566–20575 (2020).
21. S. L. Speer, W. Zheng, X. Jiang, I. T. Chu, A. J. Guseman, M. Liu, G. J. Pielak, C. Li, The intracellular environment affects protein-protein interactions. *Proc. Natl. Acad. Sci. U.S.A.* **118**, e2019918118 (2021).
22. C. M. Davis, M. Gruebele, Cellular sticking can strongly reduce complex binding by speeding dissociation. *J. Phys. Chem. B* **125**, 3815–3823 (2021).
23. I. T. Chu, C. J. Stewart, S. L. Speer, G. J. Pielak, A difference between in vitro and in-cell protein dimer formation. *Biochemistry* **61**, 409–412 (2022).
24. F. X. Theillet, In-cell structural biology by NMR: The benefits of the atomic scale. *Chem. Rev.* **122**, 9497–9570 (2022).
25. F.-X. Theillet, A. Binolfi, B. Bekei, A. Martorana, H. M. Rose, M. Stuiver, S. Verzini, D. Lorenz, M. van Rossum, D. Goldfarb, P. Selenko, Structural disorder of monomeric α-synuclein persists in mammalian cells. *Nature* **530**, 45–50 (2016).
26. D. Sakakibara, A. Sasaki, T. Ikeya, J. Hamatsu, T. Hanashima, M. Mishima, M. Yoshimasu, N. Hayashi, T. Mikawa, M. Wälchli, B. O. Smith, M. Shirakawa, P. Güntert, Y. Ito, Protein structure determination in living cells by in-cell NMR spectroscopy. *Nature* **458**, 102–105 (2009).
27. T. Tanaka, T. Ikeya, H. Kamoshida, Y. Suemoto, M. Mishima, M. Shirakawa, P. Güntert, Y. Ito, High-resolution protein 3D structure determination in living eukaryotic cells. *Angew. Chem. Int. Ed. Engl.* **58**, 7284–7288 (2019).
28. T. Muntener, D. Haussinger, P. Selenko, F. X. Theillet, In-cell protein structures from 2D NMR experiments. *J. Phys. Chem. Lett.* **7**, 2821–2825 (2016).
29. B. B. Pan, F. Yang, Y. Ye, Q. Wu, C. Li, T. Huber, X. C. Su, 3D structure determination of a protein in living cells using paramagnetic NMR spectroscopy. *Chem. Commun.* **52**, 10237–10240 (2016).
30. A. G. Palmer III, Enzyme dynamics from NMR spectroscopy. *Acc. Chem. Res.* **48**, 457–465 (2015).
31. E. Papaleo, G. Saladino, M. Lambrughi, K. Lindorff-Larsen, F. L. Gervasio, R. Nussinov, The role of protein loops and linkers in conformational dynamics and allostery. *Chem. Rev.* **116**, 6391–6423 (2016).
32. K. Bertrand, S. Reverdatto, D. S. Burz, R. Zitomer, A. Shekhtman, Structure of proteins in eukaryotic compartments. *J. Am. Chem. Soc.* **134**, 12798–12806 (2012).
33. J. Danielsson, K. Inomata, S. Murayama, H. Tochio, L. Lang, M. Shirakawa, M. Oliveberg, Pruning the ALS-associated protein SOD1 for in-cell NMR. *J. Am. Chem. Soc.* **135**, 10266–10269 (2013).
34. L. Banci, L. Barbieri, I. Bertini, E. Luchinat, E. Secci, Y. Zhao, A. R. Aricescu, Atomic-resolution monitoring of protein maturation in live human cells by NMR. *Nat. Chem. Biol.* **9**, 297–299 (2013).
35. S. Majumder, J. Xue, C. M. DeMott, S. Reverdatto, D. S. Burz, A. Shekhtman, Probing protein quinary interactions by in-cell nuclear magnetic resonance spectroscopy. *Biochemistry* **54**, 2727–2738 (2015).
36. A. Binolfi, A. Limatola, S. Verzini, J. Kosten, F. X. Theillet, H. May Rose, B. Bekei, M. Stuiver, M. van Rossum, P. Selenko, Intracellular repair of oxidation-damaged α-synuclein fails to target C-terminal modification sites. *Nat. Commun.* **7**, 10251 (2016).
37. S. Lee, H. Wen, J. W. Cha, S. Park, Specific detection of cellular glutamine hydrolysis in live cells using HNCO triple resonance NMR. *ACS Chem. Biol.* **11**, 3140–3145 (2016).
38. C. M. DeMott, R. Girardin, J. Cobbert, S. Reverdatto, D. S. Burz, K. McDonough, A. Shekhtman, Potent inhibitors of mycobacterium tuberculosis growth identified by using in-cell NMR-based screening. *ACS Chem. Biol.* **13**, 733–741 (2018).
39. A. Mochizuki, A. Saso, Q. Zhao, S. Kubo, N. Nishida, I. Shimada, Balanced regulation of redox status of intracellular thioredoxin revealed by in-cell NMR. *J. Am. Chem. Soc.* **140**, 3784–3790 (2018).
40. R. Feng, M. Gruebele, C. M. Davis, Quantifying protein dynamics and stability in a living organism. *Nat. Commun.* **10**, 1179 (2019).
41. X. C. Su, J. L. Chen, Site-specific tagging of proteins with paramagnetic ions for determination of protein structures in solution and in cells. *Acc. Chem. Res.* **52**, 1675–1686 (2019).
42. E. Luchinat, L. Barbieri, M. Cremonini, A. Nocentini, C. T. Supuran, L. Banci, Drug screening in human cells by NMR spectroscopy allows the early assessment of drug potency. *Angew. Chem. Int. Ed. Engl.* **59**, 6535–6539 (2020).
43. E. Luchinat, L. Barbieri, T. F. Campbell, L. Banci, Real-time quantitative in-cell NMR: Ligand binding and protein oxidation monitored in human cells using multivariate curve resolution. *Anal. Chem.* **92**, 9997–10006 (2020).
44. P. Broft, S. Dzatko, M. Krafcikova, A. Wacker, R. Hänsel-Hertsch, V. Dötsch, L. Trantirek, H. Schwalbe, In-cell NMR spectroscopy of functional riboswitch aptamers in eukaryotic cells. *Angew. Chem. Int. Ed. Engl.* **60**, 865–872 (2021).
45. N. Samanta, S. S. Ribeiro, M. Becker, E. Laborie, R. Pollak, S. Timr, F. Sterpone, S. Ebbinghaus, Sequestration of proteins in stress granules relies on the in-cell but not the in vitro folding stability. *J. Am. Chem. Soc.* **143**, 19909–19918 (2021).
46. A. Poulhazan, M. C. Dickwella Widanage, A. Muszyński, A. A. Arnold, D. E. Warschawski, P. Azadi, I. Marcotte, T. Wang, Identification and quantification of glycans in whole cells:

Architecture of microalgal polysaccharides described by solid-state nuclear magnetic resonance. *J. Am. Chem. Soc.* **143**, 19374–19388 (2021).
47. A. Bertarello, P. Berruyer, M. Artelsmair, C. S. Elmore, S. Heydarkhan-Hagvall, M. Schade, E. Chiarparin, S. Schantz, L. Emsley, In-cell quantification of drugs by magic-angle spinning dynamic nuclear polarization NMR. *J. Am. Chem. Soc.* **144**, 6734–6741 (2022).
48. E. Luchinat, M. Cremonini, L. Banci, Radio signals from live cells: The coming of age of in-cell solution NMR. *Chem. Rev.* **122**, 9267–9306 (2022).
49. H. Y. Carr, E. M. Purcell, Effects of diffusion on free precession in nuclear magnetic resonance experiments. *Phys. Rev.* **94**, 630–638 (1954).
50. S. Meiboom, D. Gill, Modified spin-echo method for measuring nuclear relaxation times. *Rev. Sci. Instrum.* **29**, 688–691 (1958).
51. A. G. Palmer 3rd, C. D. Kroenke, J. P. Loria, Nuclear magnetic resonance methods for quantifying microsecond-to-millisecond motions in biological macromolecules. *Meth. Enzymol.* **339**, 204–238 (2001).
52. G. N. B. Yip, E. R. P. Zuiderweg, A phase cycle scheme that significantly suppresses offset-dependent artifacts in the R2-CPMG 15N relaxation experiment. *J. Magn. Reson.* **171**, 25–36 (2004).
53. D. Long, M. L. Liu, D. W. Yang, Accurately probing slow motions on millisecond timescales with a robust NMR relaxation experiment. *J. Am. Chem. Soc.* **130**, 2432–2433 (2008).
54. X. F. Song, T. H. Lv, J. F. Chen, J. Wang, L. S. Yao, Characterization of residue specific protein folding and unfolding dynamics in cells. *J. Am. Chem. Soc.* **141**, 11363–11366 (2019).
55. G. Lipari, A. Szabo, Model-free approach to the interpretation of nuclear magnetic resonance relaxation in macromolecules. 1. Theory and range of validity. *J. Am. Chem. Soc.* **104**, 4546–4559 (1982).
56. G. Lipari, A. Szabo, Model-free approach to the interpretation of nuclear magnetic resonance relaxation in macromolecules. 2. Analysis of experimental results. *J. Am. Chem. Soc.* **104**, 4559–4570 (1982).
57. V. A. Jarymowycz, M. J. Stone, Fast time scale dynamics of protein backbones: NMR relaxation methods, applications, and functional consequences. *Chem. Rev.* **106**, 1624–1671 (2006).
58. M. Xie, L. Yu, L. Bruschweiler-Li, X. Xiang, A. L. Hansen, R. Brüschweiler, Functional protein dynamics on uncharted time scales detected by nanoparticle-assisted NMR spin relaxation. *Sci. Adv.* **5**, eaax5560 (2019).
59. S. Wardenfelt, X. Xiang, M. Xie, L. Yu, L. Bruschweiler-Li, R. Brüschweiler, Broadband dynamics of ubiquitin by anionic and cationic nanoparticle assisted NMR spin relaxation. *Angew. Chem. Int. Ed. Engl.* **60**, 148–152 (2021).
60. X. Xiang, A. L. Hansen, L. Yu, G. Jameson, L. Bruschweiler-Li, C. Yuan, R. Brüschweiler, Observation of sub-microsecond protein methyl-side chain dynamics by nanoparticle-assisted NMR spin relaxation. *J. Am. Chem. Soc.* **143**, 13593–13604 (2021).
61. M. Xie, D. W. Li, J. Yuan, A. L. Hansen, R. Bruschweiler, Quantitative binding behavior of intrinsically disordered proteins to nanoparticle surfaces at individual residue level. *Chemistry* **24**, 16997–17001 (2018).
62. J. B. Hall, D. Fushman, Characterization of the overall and local dynamics of a protein with intermediate rotational anisotropy: Differentiating between conformational exchange and anisotropic diffusion in the B3 domain of protein G. *J. Biomol. NMR* **27**, 261–275 (2003).
63. L. Yao, B. Vogeli, D. A. Torchia, A. Bax, Simultaneous NMR study of protein structure and dynamics using conservative mutagenesis. *J. Phys. Chem. B* **112**, 6045–6056 (2008).
64. Y. F. Wang, L. Y. An, Y. Yang, L. S. Yao, Generating five independent molecular alignments for simultaneous protein structure and dynamics determination using nuclear magnetic resonance spectroscopy. *Anal. Chem.* **92**, 15263–15269 (2020).
65. S. Grzesiek, A. Bax, The importance of not saturating water in protein NMR. Application to sensitivity enhancement and NOE measurements. *J. Am. Chem. Soc.* **115**, 12593–12594 (1993).
66. F. A. A. Mulder, R. A. de Graaf, R. Kaptein, R. Boelens, An off-resonance rotating frame relaxation experiment for the investigation of macromolecular dynamics using adiabatic rotations. *J. Magn. Reson.* **131**, 351–357 (1998).
67. X. Song, M. Wang, X. Chen, X. Zhang, Y. Yang, Z. Liu, L. Yao, Quantifying protein electrostatic interactions in cells by nuclear magnetic resonance spectroscopy. *J. Am. Chem. Soc.* **143**, 19606–19613 (2021).
68. S. Leeb, F. Yang, M. Oliveberg, J. Danielsson, Connecting longitudinal and transverse relaxation rates in live-cell NMR. *J. Phys. Chem. B* **124**, 10698–10707 (2020).
69. Y. Ye, X. Liu, Z. Zhang, Q. Wu, B. Jiang, L. Jiang, X. Zhang, M. Liu, G. J. Pielak, C. Li, (19) F NMR spectroscopy as a probe of cytoplasmic viscosity and weak protein interactions in living cells. *Chemistry* **19**, 12705–12710 (2013).
70. E. Chen, R. M. Esquerra, P. A. Melendez, S. S. Chandrasekaran, D. S. Kliger, Microviscosity in *E. coli* cells from time-resolved linear dichroism measurements. *J. Phys. Chem. B* **122**, 11381–11389 (2018).
71. G. Jameson, R. Bruschweiler, NMR spin relaxation theory of biomolecules undergoing highly asymmetric exchange with large interaction partners. *J. Chem. Theory Comput.* **17**, 2374–2382 (2021).
72. M. R. Hansen, L. Mueller, A. Pardi, Tunable alignment of macromolecules by filamentous phage yields dipolar coupling interactions. *Nat. Struct. Biol.* **5**, 1065–1074 (1998).
73. D. W. Li, M. Z. Xie, R. Bruschweiler, Quantitative cooperative binding model for intrinsically disordered proteins interacting with nanomaterials. *J. Am. Chem. Soc.* **142**, 10730–10738 (2020).
74. L. E. Hough, K. Dutta, S. Sparks, D. B. Temel, A. Kamal, J. Tetenbaum-Novatt, M. P. Rout, D. Cowburn, The molecular mechanism of nuclear transport revealed by atomic-scale measurements. *eLife* **4**, e10027 (2015).
75. N. Salvi, A. Abyzov, M. Blackledge, Atomic resolution conformational dynamics of intrinsically disordered proteins from NMR spin relaxation. *Prog. Nucl. Magn. Reson. Spectrosc.* **102-103**, 43–60 (2017).
76. J. T. Mika, B. Poolman, Macromolecule diffusion and confinement in prokaryotic cells. *Curr. Opin. Biotechnol.* **22**, 117–126 (2011).
77. N. Zhang, Y. Wang, L. An, X. Song, Q. Huang, Z. Liu, L. Yao, Entropy drives the formation of salt bridges in the protein GB3. *Angew. Chem. Int. Ed. Engl.* **56**, 7601–7604 (2017).
78. S. Grzesiek, A. Bax, An efficient experiment for sequential backbone assignment of medium-sized isotopically enriched proteins. *J. Magn. Reson.* **99**, 201–207 (1992).
79. X. F. Song, L. An, M. Wang, J. Chen, Z. Liu, L. Yao, Osmolytes can destabilize proteins in cells by modulating electrostatics and quinary interactions. *ACS Chem. Biol.* **16**, 864–871 (2021).
80. L. Yao, J. Ying, A. Bax, Improved accuracy of 15N–1H scalar and residual dipolar couplings from gradient-enhanced IPAP-HSQC experiments on protonated proteins. *J. Biomol. NMR* **43**, 161–170 (2009).
81. G. M. Clore, A. Szabo, A. Bax, L. E. Kay, P. C. Driscoll, A. M. Gronenborn, Deviations from the simple two-parameter model-free approach to the interpretation of nitrogen-15 nuclear magnetic relaxation of proteins. *J. Am. Chem. Soc.* **112**, 4989–4991 (1990).
82. L. S. Yao, A. Grishaev, G. Cornilescu, A. Bax, Site-specific backbone amide ^{15}N chemical shift anisotropy tensors in a small protein from liquid crystal and cross-correlated relaxation measurements. *J. Am. Chem. Soc.* **132**, 4295–4309 (2010).
83. B. Hess, C. Kutzner, D. van der Spoel, E. Lindahl, GROMACS 4: Algorithms for highly efficient, load-balanced, and scalable molecular simulation. *J. Chem. Theory Comput.* **4**, 435–447 (2008).
84. O. F. Lange, N. A. Lakomek, C. Farès, G. F. Schröder, K. F. A. Walter, S. Becker, J. Meiler, H. Grubmüller, C. Griesinger, B. L. de Groot, Recognition dynamics up to microseconds revealed from an RDC-derived ubiquitin ensemble in solution. *Science* **320**, 1471–1475 (2008).
85. P. S. Huang, Y. E. A. Ban, F. Richter, I. Andre, R. Vernon, W. R. Schief, D. Baker, RosettaRemodel: A generalized framework for flexible backbone protein design. *PLOS ONE* **6**, e24109 (2011).
86. D. C. Chatfield, A. Szabo, B. R. Brooks, Molecular dynamics of staphylococcal nuclease: Comparison of simulation with ^{15}N and 13C NMR relaxation data. *J. Am. Chem. Soc.* **120**, 5301–5311 (1998).
87. T. S. Ulmer, B. E. Ramirez, F. Delaglio, A. Bax, Evaluation of backbone proton positions and dynamics in a small protein by liquid crystal NMR spectroscopy. *J. Am. Chem. Soc.* **125**, 9179–9191 (2003).
88. A. Abragam, *The Principles of Nuclear Magnetism* (Clarendon Press, 1961).

Acknowledgments: We thank W. Zhan for arranging NMR time. **Funding:** This work was supported by the National Key R&D Program of China (grant no. 2022YFC2104701 to L.Y.), the National Natural Science Foundation of China (grant nos. 32171229 to X.S. and 32271268 to L.Y.), the Shandong Provincial Natural Science Foundation (grant no. ZR2020MC010 to X.S.), the Taishan Scholars Program of Shandong Province (grant no. ts201712077 to L.Y.), the Youth Innovation Promotion Association of the CAS (grant number 2020216 to X.S.), and the Shandong Energy Institute (SEI) (grant nos. SEI I202145 to X.S. and SEI S202105 to L.Y.). A portion of this work was performed on the National Facility for Protein Science Shanghai, Zhangjiang Lab. **Author contributions:** L.Y. designed research; M.W., X.S., J.C., X.C., X.Z., Y.Y., and Z.L. performed research; M.W., X.S., J.C., and L.Y. analyzed data; and M.W., X.S., and L.Y. wrote the paper. **Competing interests:** The authors declare that they have no competing interests. **Data and materials availability:** All data needed to evaluate the conclusions in the paper are present in the paper and/or the Supplementary Materials. The codes for model-free and CPMG data analyses are available at https://doi.org/10.6084/m9.figshare.22324963.v1.

Submitted 5 February 2023
Accepted 21 June 2023
Published 21 July 2023
10.1126/sciadv.adg9141